ARTICLE OPEN

Photo-tunable transfer characteristics in $MoTe_2$–MoS_2 vertical heterostructure

Arup Kumar Paul[1], Manabendra Kuiri[1], Dipankar Saha[2], Biswanath Chakraborty[1], Santanu Mahapatra[2], A. K Sood[1] and Anindya Das[1]

Fabrication of the out-of-plane atomically sharp p–n junction by stacking two dissimilar two-dimensional materials could lead to new and exciting physical phenomena. The control and tunability of the interlayer carrier transport in these p–n junctions have a potential to exhibit new kind of electronic and optoelectronic devices. In this article, we present the fabrication, electrical, and opto-electrical characterization of vertically stacked few-layers $MoTe_2$(p)–single-layer MoS_2(n) heterojunction. Over and above the antiambipolar transfer characteristics observed similar to other hetero p–n junction, our experiments reveal a unique feature as a dip in transconductance near the maximum. We further observe that the modulation of the dip in the transconductance depends on the doping concentration of the two-dimensional flakes and also on the power density of the incident light. We also demonstrate high photo-responsivity of ~10^5 A/W at room temperature for a forward bias of 1.5 V. We explain these new findings based on interlayer recombination rate-dependent semi-classical transport model. We further develop first principles-based atomistic model to explore the charge carrier transport through $MoTe_2$–MoS_2 heterojunction. The similar dip is also observed in the transmission spectrum when calculated using density functional theory–non-equilibrium Green's function formalism. Our findings may pave the way for better understanding of atomically thin interface physics and device applications.

npj 2D Materials and Applications (2017)1:17 ; doi:10.1038/s41699-017-0017-3

INTRODUCTION

In recent years, van der Waals (vdW) heterostructures based on transition metal dichalcogenides (TMDs) are being studied extensively, due to their excellent electronic and opto-electronic properties[1–4] with potential applications such as transistor,[5] photo detector,[6, 7] light-emitting diode (LED),[8–10] and solar cells.[11, 12] Atomically sharp interfaces with intralayer high carrier mobility and lack of dangling bonds result in unique spatial charge separation[13] between the layers, as well as produce long-lived interlayer excitons[14] under light exposure. These TMD-based vertical heterostructures have shown potentials as p–n junction and most of these p–n junctions show antiambipolar transconductance behavior.[15–21] However, p–n junction made of single layer of TMDs, known as atomically thin p–n junctions,[22–25] show quite different type of charge transport mechanism compared to the conventional p–n junction. Here, transport occurs via tunneling of carriers from one layer to the other layer.[6, 25] This tunneling at the interfaces is predicted to be governed by Shockley-Read-Hall (SRH) or by Langevin recombination mechanisms.[25] The band engineering of vertical heterostructures[26] with available TMDs having different band gaps and work functions have paved the way to investigate the charge transport mechanisms in atomically thin p–n junction.

In this work, we have carried out electrical and photo-conductivity measurements of vertical heterostructures made of a few-layers $MoTe_2$ (~6 layers) and single-layer MoS_2. The junction current (I_{DS}) vs. bias (V_{DS}) data show the characteristics of a p–n junction. Interestingly, the I_{DS} as a function of back gate voltage (V_{BG}) show an unusual dip at the highest conductance value on top of the usual antiambipolar nature.[15–21] We further show that the magnitude and the position of the dip in I_{DS}–V_{BG} curve can be modulated by changing the incident power density of light. This unique observation can be explained by including interlayer recombination rate of charge carriers along with the individual layer response. We also report very high photo-responsivity of ~10^5 A/W under forward bias 1.5 V at room temperature. It is seen that the photo-responsivity for blue (450 nm) and red (650 nm) light is few orders of magnitude higher than near infrared (IR) (850 nm) light. We have further carried out first principles-based density functional theory (DFT)- nonequilibrium Green's function (NEGF) calculations, which do capture the evolution of the above mentioned dip.

RESULTS

Experimental results without light

The schematic of the device and the experimental setup are shown in Fig. 1a. Oxidized silicon wafer with 285-nm thick SiO_2 layer was used as a substrate for the heterojunction devices. Few-layer $MoTe_2$ was exfoliated on the wafer, followed by transfer of a single-layer MoS_2 flake using well-known polydimethylsiloxane (PDMS) dry transfer technique.[27] The metal contacts on individual flakes were made using standard e-beam lithography, followed by thermal deposition of Ti/Au contacts (5/70 nm). For the electrical measurements, DC bias (V_{DS}) was applied and the output current (I_{DS}) was measured with a current amplifier as shown in Fig. 1a. In order to change the carrier concentration, the gate voltage (V_{BG}) was applied to the P^{++} Si substrate. The fabrication details as well as measurement details have been mentioned in the "Methods" section. Figure 1b shows the optical as well as atomic force microscope (AFM) image of one of the devices, termed as *D*1. As

[1]Department of Physics, Indian Institute of Science, Bangalore 560012, India and [2]Department of Electronic Systems Engineering, Indian Institute of Science, Bangalore 560012, India
Correspondence: Anindya Das (dasanindy@gmail.com)

Received: 9 December 2016 Revised: 25 May 2017 Accepted: 30 May 2017
Published online: 27 June 2017

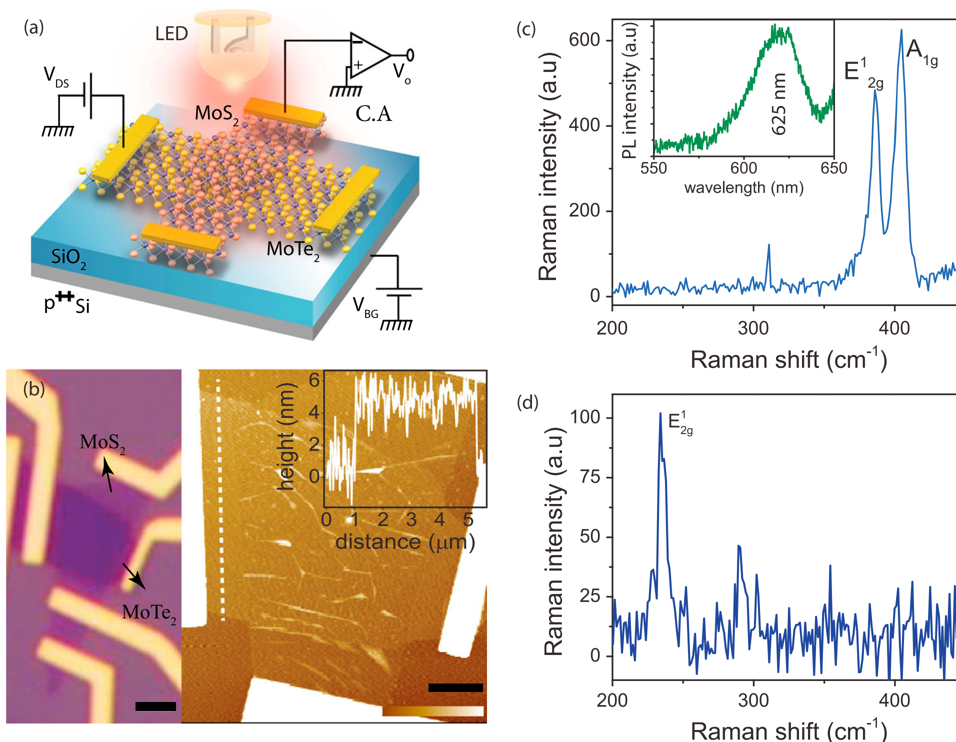

Fig. 1 **a** Schematics of the device, with the experimental setup. Bias (V_{DS}) was applied to $MoTe_2$ flake and current output was measured with a current amplifier (CA) connected to MoS_2 flake. Gate voltage (V_{BG}) was applied to P^{++} Si of the substrate. LED was used to illuminate the sample for opto-electronics measurements. **b** Optical image (*left*) and AFM image (*right*) of the device. The scale bar (*black*) for optical and AFM images are, respectively, 2 µm and 1 µm. The color scale bar for AFM image is 85 nm. *Inset* is $MoTe_2$ height profile along the *dashed line*. **c** Raman and PL (*inset*) of MoS_2. **d** Raman for $MoTe_2$

seen in Fig. 1b, the measured height of the $MoTe_2$ flake was 4 nm, corresponding to six layers.[28, 29] Figure 1d depicts the Raman spectra of the $MoTe_2$ flake, which shows the characteristic in plane E^1_{2g} peak at 234 cm^{-1}.[24–29] The Raman spectra for MoS_2 flake is shown in Fig. 1c. Here, the MoS_2 characteristic E^1_{2g} and out of plane A_{2g} peaks can be seen, respectively, at 386 and 405 cm^{-1}. The inset of Fig. 1c shows the MoS_2 photoluminescence (PL) spectra, which shows a single peak near 625 nm. Both Raman and PL verifies that the MoS_2 flake is a single layer.[30, 31]

Electrical and opto-electronic measurements were performed at room temperature in a vacuum of 10^{-5} mbar on seven devices. Though the responses were similar in all the devices, the magnitude of the response varied from sample to sample, depending on the quality of the contacts as well as the quality of the heterojunction interface. Here, we discuss four devices, for which best results were obtained. Figure 2a shows conductance (G) as a function of V_{BG} for individual MoS_2 (*red curve*) and $MoTe_2$ (*blue curve*) for the $D1$ device. As can be seen in Fig. 2a, MoS_2 flake is n-doped with a threshold voltage (V_{th}) ~−20 V and $MoTe_2$ flake is p-doped with V_{th} ~+5 V. The I_{DS}–V_{DS} response of individual flakes, shown in the Supplementary Information (SI), indicates absence of any significant Schottky barriers at the contacts. Figure 2b displays the I_{DS}–V_{DS} response of the junction for several V_{BG}, showing rectification behavior, expected for the p–n junction at the interface. Even though the observed I_{DS}–V_{DS} curve is qualitatively similar to a conventional p–n junction, the current does not increase exponentially with forward bias; rather, it increases almost linearly, pointing to the underlying rectification mechanism being different.[25] The I_{DS}–V_{BG} plots for different V_{DS} are shown in Fig. 2c. The overall antiambipolar shape of the curves can be understood qualitatively by considering the resistances of MoS_2 and $MoTe_2$ parts in series. At large positive V_{BG}($V_{BG} > 20$ V) and negative V_{BG}($V_{BG} < -20$ V) the current is very small, as one of the layer goes to the insulating state. The current is maximum near V_{BG} ~−10 V, as expected from the conductance of individual layers seen in Fig. 2a. Though this series resistance model is able to explain the antiambipolar nature of the transconductance, it is inadequate to explain the unusual dip near the conductance maximum near −10 V. *Inset* of Fig. 2c shows the I_{DS}–V_{BG} response from yet another device ($D2$), which also shows similar dip near the conductance maximum (V_{BG} ~−13 V). However, for $D3$ and $D4$ devices (Fig. 2d) no dip was observed. In the next paragraph we will show that the dip can be tailored with the incident light. The detailed characteristics of these devices are given in SI.

Experimental results with light

To further elucidate the I_{DS}–V_{BG} curves, we have carried out the transport measurements with the exposure of light for blue (wavelength λ ~450 nm), red (λ ~650 nm), and near IR (λ ~850 nm) LEDs on the $D3$ device. It was observed that the device response changed drastically with exposure of light, and even after LED was switched off the changes were retained for a long time ~24 h. First, I_{DS}–V_{BG} measurements are made as a function of incident light intensity (in increasing order), and then with the light off gate response is measured at regular intervals of time for several hours until the response curve is same as the initial state. Similar results were obtained in repeated runs of light-on/light-off cycles. Figure 3a shows the evolution of the gate response (at V_{DS} = 1.5 V) under blue LED for the second cycle of measurements. It can be seen that with increasing light intensity the peak value of I_{DS} increases and the position of the peak systematically shifts toward higher negative gate voltages. This shift of position (ΔV_{BG}) of peak I_{DS} as a function of power density is shown in Fig. 3d (*green curve*). As can be seen in Fig. 3a, the V_{th} on the left side of the peak moves toward more negative V_{BG} without affecting significantly the V_{th} on the right side. This suggests that with increasing light intensity the MoS_2 flake gets

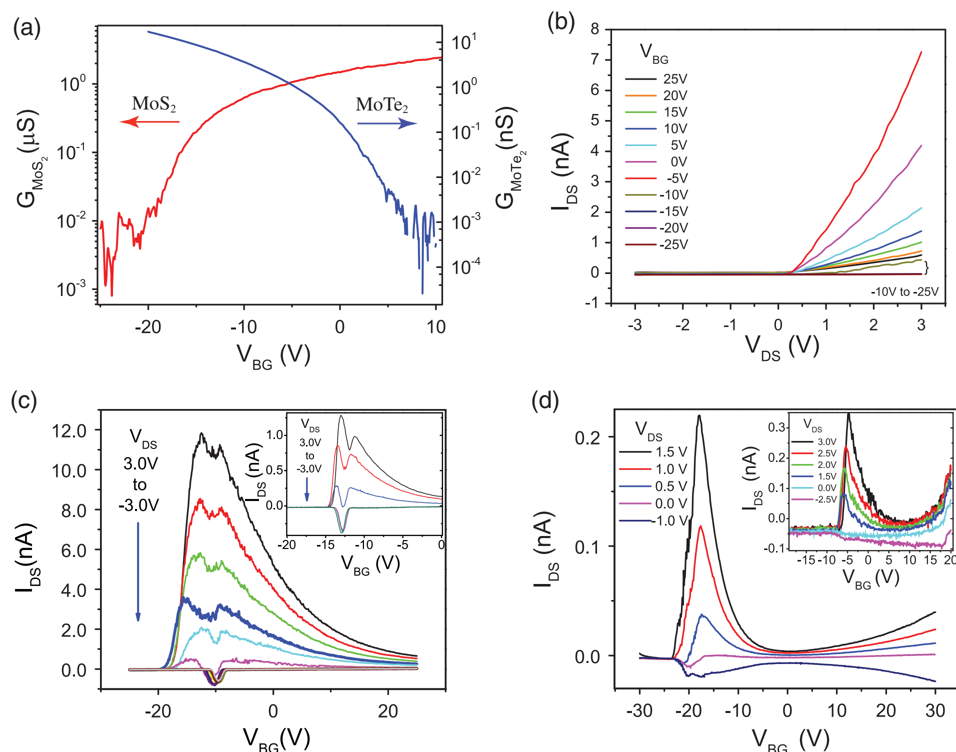

Fig. 2 **a** Gate response of individual MoS_2 (*red curve*) and $MoTe_2$ (*blue curve*) for device *D*1. **b** I_{DS}–V_{DS} response of the junction. Responses for V_{BG} −20 V to −5 V shows clear rectification behavior. **c** I_{DS}–V_{BG} response of the junction from V_{DS} −3 V to +3 V in 0.5 V steps. An anomalous dip can be observed near the maximum of current in forward bias. *Inset* shows I_{DS}–V_{BG} response for device *D*2. Here also similar dip can be observed. **d** I_{DS}–V_{BG} response for device *D*3 and *inset* shows the same for device *D*4. No dip was observed for *D*3 and *D*4

more n-doped, while the change in $MoTe_2$ doping is very small. Most interestingly, the dip in gate response curve near the maximum I_{DS} starts appearing with increasing optical power and then vanishes at higher light intensities. In the *inset* of Fig. 3a, we show gate response for three different light intensities during the first cycle of the measurement. The magnitude of the dip (ΔI_{DIP}) as a function of power density is plotted in Fig. 3d (*blue curve*). A comparison of I_{DS}–V_{DS} characteristics under dark and illuminated condition at $V_{BG} = -30$ V has been shown in Fig. 3b. The overall I_{DS}–V_{DS} curve under illumination is similar to that of the device in on-state (SI). It may be noted that the device goes from completely off-state to on-state with light. This behavior could be understood as following: at $V_{BG} = -30$ V the junction does not conduct in dark state because MoS_2 is completely depleted and starts conducting on light exposure, as MoS_2 gets doped. *Inset* of Fig. 3b shows the response of the device (at $V_{DS} = 1$ V, $V_{BG} = -30$ V) to a very short light pulse. Though switching time from off to on state is less than ~600 mS (limited by our measuring instrument), the device shows a strong memory effect as I_{DS} reduces slowly with time. In Fig. 3c, the evolution of gate response with time is shown after the LED was switched off (LED off part of the second cycle) and it takes almost a day for the response to come back to its initial condition. Interestingly, here also we see the dip appearing and again disappearing with time. The quantitative measure of ΔI_{DIP} with time has been plotted in Fig. 3e.

Photo-responsivity

Similar to the results for blue LED shown in Fig. 3, the experiments were performed with red and IR LEDs. The overall transconductance behavior of the device was similar, except for the magnitude of I_{DS}, for all the LEDs, as shown in Fig. 4a. I_{ph} is taken as the difference of I_{peak} of the gate response under illumination to the corresponding I_{DS} in gate response without illumination. As shown in Fig. 4a, I_{ph} is maximum for the red light. In SI Fig. S5 I_{DS}–V_{DS} responses under dark and illuminated condition has been compared for several V_{BG}, which shows the dependence of photo-responsivity on V_{DS}. The highest photo response is achieved at $V_{DS} = 1.5$ V, which has been plotted in Fig. 4b. The nature of plots is very similar to MoS_2-graphene heterostructures.[32] As can be seen, for red and blue light, photo-responsivity ~10^5 A/W has been achieved. For IR light (1.45 eV), the photo-responsivity is several orders of smaller (Fig. 4b) as the photon energy is below the band gap of single-layer MoS_2.

DISCUSSION

Understanding the dip in photo response within a classical model

We use the interlayer recombination model[25] to understand the results presented in Fig. 3. Under forward bias the charge carriers conduct via tunneling-mediated interlayer recombination as $I_{DS} \propto R_C V_{DS}$, where R_C is the recombination rate. R_C is proportional to n_{eff}/τ, where n_{eff} is effective carrier concentration and τ is interlayer tunneling time. Here, $n_{eff} = n_S p_T/(n_S + p_T)$, where n_S and p_T are the electron and hole concentrations of individual flakes, which are tuned by gate voltage as well as light intensity. In Fig. 5, the effect of photo-doping on R_C has been discussed. Here, we have used the SRH mechanism for R_C.[25] However, similar kind of transport characteristics can be obtained from Langevin processes.[25] The photo-induced doping mechanism has been illustrated schematically in Fig. 5a, where the gate voltage drops mostly across the SiO_2 layer and few-layers $MoTe_2$. The incident photons create electron-hole pairs in both MoS_2 and $MoTe_2$, but due to the presence of electric field (negative V_{BG}) the excited electrons (holes) will move toward the MoS_2 layer ($MoTe_2$–SiO_2 interface), moving the Fermi level in MoS_2 closer to the conduction band (Fig. 5a). However, the photo-excited holes in $MoTe_2$ get trapped mostly at the $MoTe_2$–SiO_2 interface as well as at the defect states inside the $MoTe_2$ closer to its valence band, which are mostly immobile (reflected in poor mobility <1 cm^2/Vs)

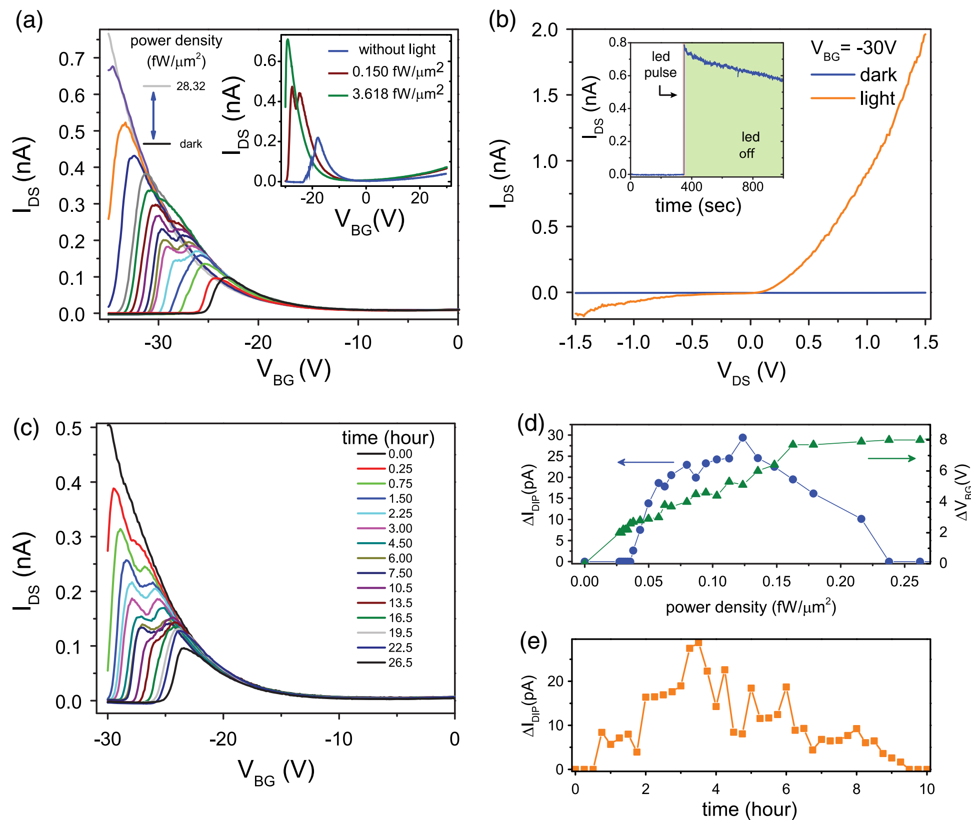

Fig. 3 **a** Evolution of I_{DS}–V_{BG} response of device *D*3, with increasing light intensity (*blue*) during second cycle. The dip can be seen appearing and again disappearing with increasing optical power. *Inset* shows evolution of I_{DS}–V_{BG} during first cycle. **b** Comparison of I_{DS}–V_{DS} response under dark and illuminated condition. *Inset* shows led pulse experiment, which shows memory effect. **c** Evolution of I_{DS}–V_{BG} with time after led was switched off. Here also the dip can be seen appearing after few hours, and then again vanishing. **d**, **e** Evolution of dip magnitude (ΔI_{DIP}) with optical power density and time

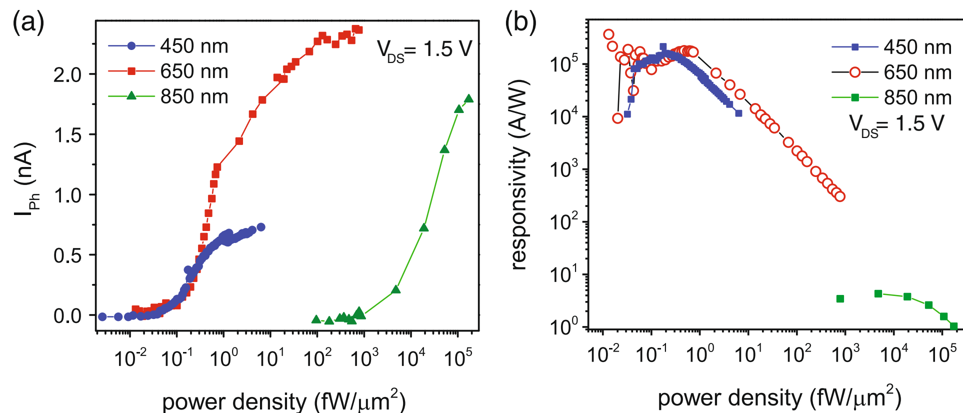

Fig. 4 For device *D*3. **a** Photo current (I_{ph}) as function of optical power density for red (*red curve*), blue (*blue curve*), and IR (*green curve*) lEDs. **b** Photo-responsivity for red, blue, and IR light at $V_{DS} = 1.5$ V. Though for red and blue the photo-responsivity was similar and of the order of 10^5 A/W, for IR it is several orders of magnitude small

and hence do not participate in conduction.[32–35] This also explains why it takes almost a day to come back to its initial value after the light is off (Fig. 3c). The photo-induced effect has been quantitatively presented in Fig. 5b. The induced carrier concentration (n) as a function of V_{BG} in MoS_2 and $MoTe_2$ has been generated using capacitive model, $n = n_0 + C_G(V_{BG} - V_{th})/e$, where C_G is the geometrical capacitance and n_0 is the majority carrier concentration due to trap and defect states for $V_{BG} < V_{th}$. In this model, we have taken $n_0 = 3 \times 10^{13}$ m^{-2}, which is similar to ref. 25. With increasing optical power density we have shifted the V_{th} of MoS_2 toward left side by ΔV_{BG} comparable to the experimental values (Fig. 3d). To explain the transconductance data of our device in Fig. 3, we need to consider resistances coming from both the individual layers (non-overlapped) as well as the junction part (overlapped). However, the gate response of the individual flakes (non-overlapped) changes less significantly with light (see SI), and hence we consider only the effect of the junction. In the *bottom panel* of Fig. 5b, we have plotted R_C as a function of V_{BG} for different amount of photo-induced doping as shown in Fig. 5b (*upper panel*). This classical model qualitatively shows the

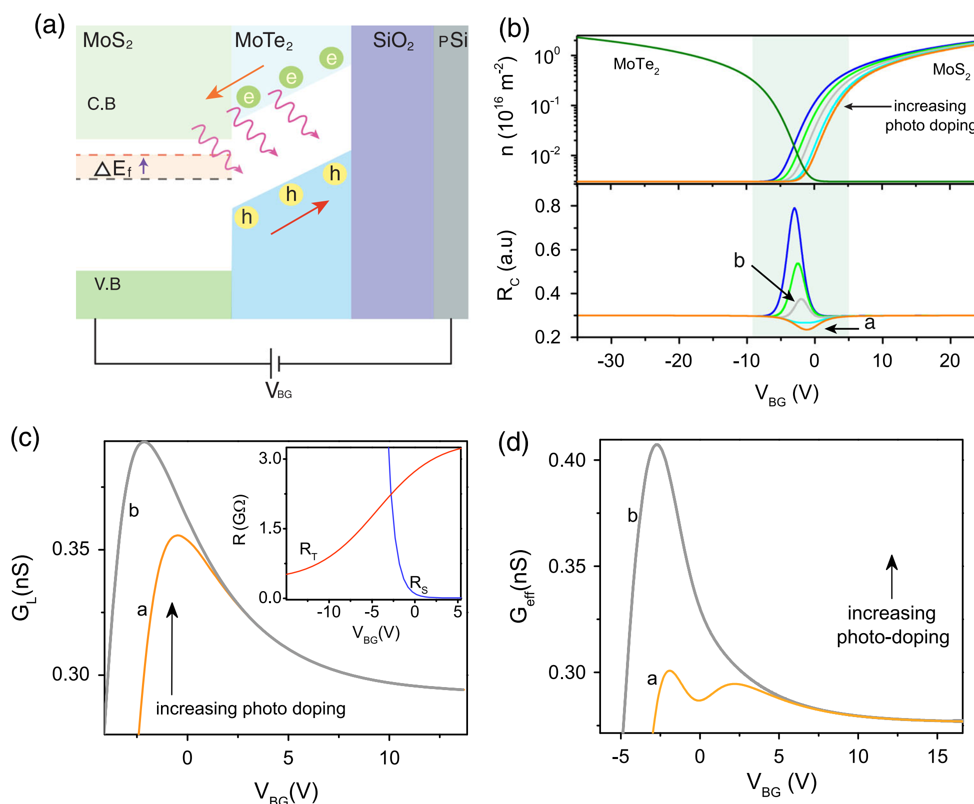

Fig. 5 **a** Schematic diagram of photo-induced doping process of MoS_2 and $MoTe_2$ flakes. **b** Capacitive model to simulate effect of photo doping on the carrier concentration of individual flakes. *Upper panel* shows carrier concentration (n) vs. V_{BG} plot for both flakes. For MoS_2, n–V_{BG} curves with different V_{th} has been plotted considering its pronounced photo-doping effect. On the other hand, one fixed n–V_{BG} has been plotted for $MoTe_2$, as it shows much less photo-doping effect. In the *lower panel*, R_C–V_{BG} graphs has been plotted for the corresponding MoS_2 n–V_{BG} curves. The curves marked by "a" and "b" are used for G_{eff} calculation. **c** G_L as function of V_{BG} for two different V_{th} of MoS_2 corresponding to the "a" and "b" n–V_{BG} curves. *Inset* shows the individual resistance R_S and R_T as functions of V_{BG}. **d** G_{eff} as function of V_{BG}. As can be seen G_{eff} captures the dip to peak transition

transformation from a dip to no-dip in the modulation of recombination rate by the photo-induced doping.

To understand how R_C influences the overall transconductance curve, we need to consider the lateral series resistance (R_L) coming from the individual flakes at junction, as well as the tunneling resistance (R_j), which is inversely proportional to R_C. R_L is equal to $R_S + R_T$, where R_S and R_T are lateral resistances coming from individual MoS_2 and $MoTe_2$, respectively. In Fig. 5c, the *inset* shows R_S and R_T as functions of V_{BG}. These have been obtained by fitting the experimental G–V_{BG} curve of MoS_2 and $MoTe_2$, respectively (for device *D*3). Figure 5c shows the plot of total lead conductance $G_L = (R_S + R_T)^{-1}$ vs. V_{BG} for two different V_{th} of MoS_2 (differing by ΔV_{BG} ~2.5 V) corresponding to the curves marked by "a" and "b" in Fig. 5b (*lower panel*). Please note that Fig. 5c does not capture the dip observed in our experiments. Next, we show the effect on the transconductance by including the series resistance R_L along with the tunneling resistance R_j. In Fig. 5d, we plot $G_{eff} = (R_L + R_j)^{-1}$ as a function V_{BG} corresponding to the same "a" and "b" curves in Fig. 5b. It can be seen that the dip can be qualitatively explained by inclusion of the interlayer recombination rate.

DFT–NEGF calculation

In order to get insights on the charge carrier transport through $MoTe_2$–MoS_2 vdW interface, we have also carried out an atomistic study[36–41] on the two port device structures as illustrated in Fig. 6. As shown in Fig. 6a, the length of the channel region (L) is taken as ~6.6 nm (along the transport direction, i.e., the Z-axis), whereas the MoS_2–$MoTe_2$ overlapping distance is maintained as ~2.2 nm (which is 1/3rd of the total channel length). Moreover, along the X-axis (perpendicular to the plane) we incorporate a vacuum region of 15 Å (sufficient to avoid any spurious interaction between periodic images). Here, the left (t_left ~16.57 Å) and the right (t_right ~16.57 Å) electrodes are acting as the semi-infinite reservoirs. Here, after we will call this device structure as vdW interface1. Besides, the zoomed region shown within dotted arrows portrays the top view of the channel of MoS_2–$MoTe_2$ vdW interface (having an width ~1 nm). The details of the calculation are given in the SI.

Next, we consider two more variants of the aforementioned device (namely, vdW interface2 and vdW interface3), where the MoS_2 and the $MoTe_2$ flakes are of doped with different doping concentrations. In ATK (Atomistix Tool Kit), the effective doping (n-type or p-type) can be achieved by means of incorporating appropriate compensation charge to the system.[42, 43] This effective doping scheme (atomic compensation charge) is really advantageous, as it does not depend either on the exact dimensions of the system or on the specific details of the dopant atoms.[42] Considering moderate and high doping densities 3.85×10^{17} cm^{-3} and 1.28×10^{19} cm^{-3}, we set the "atomic compensation charge" values,[44] which are equivalent to two-dimensional densities 2.56×10^{14} m^{-2} and 8.5×10^{15} m^{-2}, respectively. For vdW interface2 and vdW interface3, the MoS_2 flakes are n-doped, whereas the $MoTe_2$ flakes are p-doped, with the corresponding "atomic compensation charge" values. It is important to realize that, for any DFT–NEGF simulation, the electrodes act as the carrier reservoirs to maintain equilibrium for the entire system.[42] Moreover, taking vdW interface3 into consideration, we find that the energy-position resolved local density of states (LDOS) diagram (as shown in Fig. 6) clearly represents the band alignment of a type-II heterostructure.

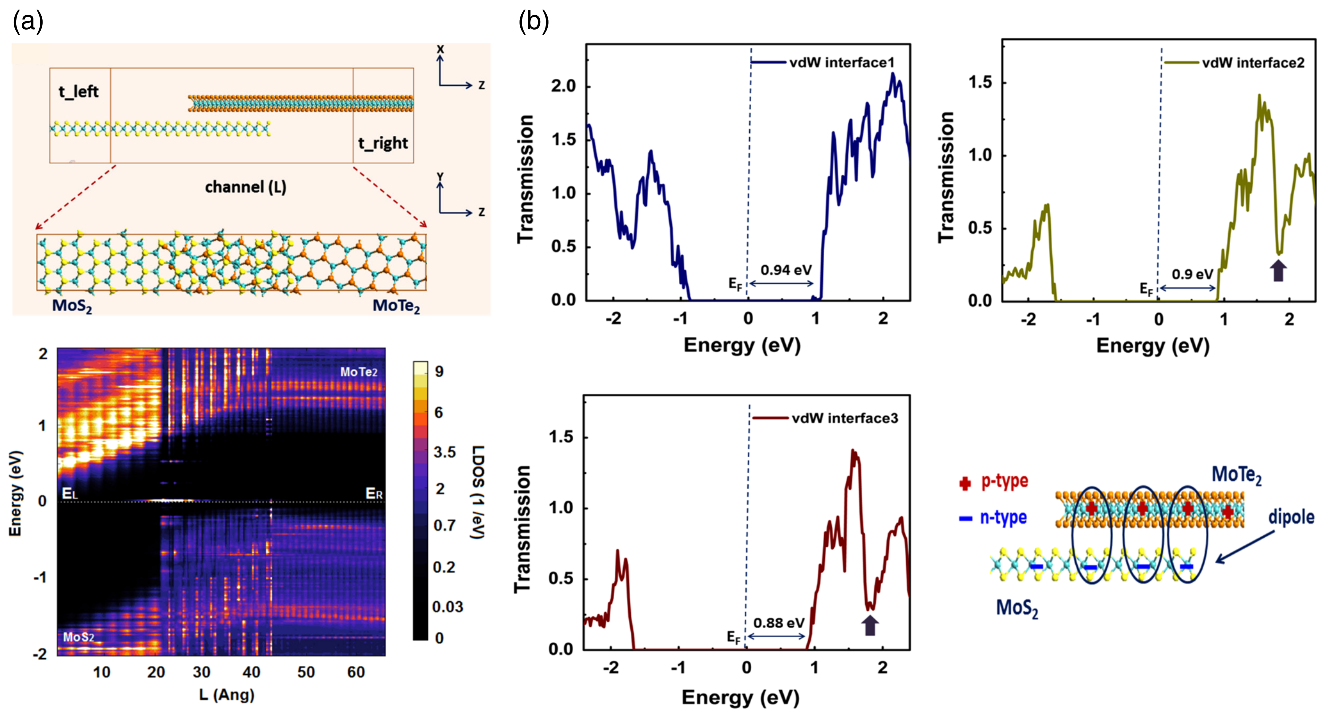

Fig. 6 **a** (*top*) $MoTe_2$–MoS_2 vdW interface, where length of the channel is ~6.6 nm and width is ~1 nm. (*bottom*) Energy-position resolved LDOS diagram for the vdW interface3. **b** Transmission spectra of vdW interface1 (*upper left*), vdW interface2 (*upper right*), and vdW interface3 (*bottom left*). (*bottom right*) The schematic illustrates the formation of electric dipoles along the channel

Figure 6b illustrates the zero bias transmission spectra of the MoS_2–$MoTe_2$ vdW interfaces. It is quite interesting to observe that the transmission spectra obtained for the vdW interface2 and vdW interface3 structures are quite different from that of the vdW interface1. For the intrinsically charge neutralized MoS_2 and $MoTe_2$ sheets of vdW interface1, we see no significant dip in states, within the positive energy range of 0 to 2 eV. However, for the samples those are effectively doped into n-type and p-type, we notice the distinct effect of charge separation. The excess negative and positive charge carriers across the individual layers (Fig. 6b, *bottom right*) give rise to strong interlayer coupling and modulates the transmission states within the range of 0–2 eV. Here, we emphasize on the positive energy transmission states of the individual vdW interfaces. It is worth mentioning that for near-equilibrium electrical current calculation, the states within the bias window ultimately matters. So for any finite bias, the states that are closer to the Fermi energy (E_F) will play the dominant role. Nonetheless, it can be seen from Fig. 6b that the states corresponding to $V.B._{max}$ have further been shifted away from the energy zero (i.e., $E - E_F = 0$) for the vdW interface2 and the vdW interface3. Considering the energy range of 0–2 eV, it is evident from Fig. 6b (*upper left*) that there will be no anomalous dip in the maximum current (at forward bias) for the vdW interface1. However, this is not the same for other device(s) with excess n-type or p-type carriers. Investigating the transmission spectra, as illustrated in Fig. 6b (*upper right* and *bottom left*), we observe clear dips (pointed by *arrows*) around 1.8 eV. A quantitative calculation of transmission spectra as a function of back gate voltage is, however, beyond the scope of our work at this stage.

To understand the physics behind the atypical nature of the transmission spectra obtained for vdW interface2 and vdW interface3, we propose a plausible explanation. It is known from the literature[13] that the excess negative and positive charge carriers across the individual layers (Fig. 6b) make interlayer electric dipoles, which could be the permanent one.[13, 14, 45] Nevertheless, this will give rise to a strong interlayer coupling, and perhaps shift-in the trenches of the transmission spectra to the lower-energy range values (which is ~1.8 eV, in this case). Even though both classical and DFT–NEFG calculations qualitatively support our observation, a complete understanding of the transformation of the dip need further theoretical work.

In summary, we demonstrate electrical and opto-electronic measurements on $MoTe_2$–MoS_2 vdW heterojunction devices. In normal transconductance measurements, some of the devices showed an anomalous dip in current near the maximum conductance state. We showed that the dip can be modulated with light intensity. We have correlated this anomalous feature within a classical model based on interlayer recombination processes, followed by electrical transport calculations using DFT–NEGF. The first principles-based quantum transport calculation qualitatively capture the anomalous feature depending on the carrier concentration of the individual flakes. Our devices also show large photo response of ~10^5 A/W at room temperature, which makes it a potential candidate for charge integrating type opto-electronic applications.

METHODS

The heterojunction devices were fabricated on Si/SiO_2 substrate with 285-nm thick SiO_2 layer. The MoS_2 and $MoTe_2$ flakes were exfoliated on PDMS and substrate, respectively, from bulk crystal using scotch tape method. To make heterojunction devices, the thinnest flakes were identified with optical microscope. Then Raman and PL spectroscopy was used to sort out single-layer MoS_2 and non-contact AFM was used to identify 6–8 layers of $MoTe_2$ flakes. All the AFM characterizations were performed with Park NX10 AFM. After transferring the MoS_2 flakes on the $MoTe_2$ flakes, the eletrical contacts were patterned using standard e-beam lithography. Then Ti/Au (5/70 nm) were deposited on the lithography-patterned sample, by thermal evaporation to realize the electrical contacts. The electrical and opto-electronic measurements were performed inside a home-built cryostat, under vacuum of 10^{-5} mbar at room temperature. For all DC characterization, Keythly 2400 source-meter, Agilent 34401A digital multimeter, and a home-built low-noise current amplifier was used. For opto-electrical measurements, the leds were fixed at ~2 mm distance from the devices. The leds were illuminated with Kythly 2400 in current source mode. The led power was calibrated with *PM*203 Thorlabs optical power meter.

Data availability

The authors declare that the main data supporting the findings of this study are available within the paper and its SI file. Other relevant data are available from the corresponding author upon request.

ACKNOWLEDGEMENTS

The device fabrication was performed using facilities at CeNSE, funded by Department of Information Technology, Govt. of India, and located at Indian Institute of Science, Bangalore. A.K.S. thanks Department of Science and Technology (DST), India for financial support. A.D. thanks DST and Indian Space Research Organization (ISRO) for financial support. This work is supported by Department of Science and Technology (DST), Government of India, under Grant No: DSTO/PPH/AYD/1470, and Indian Space Research Organization (ISRO), Government of India, under Grant No: ISTC/PPH/AYD/0343. S.M. acknowledges the support by Science and Engineering Research Board (SERB), Department of Science and Technology (DST), Government of India, under Grant No: SB/S3/EECE/0209/2015.

AUTHOR CONTRIBUTIONS

A.P., A.K.S., and A.D. conceived the idea of this research. A.D. and A.P. together designed the experimental setup. A.P. performed the heterojunction device fabrication, electrical and opto-electronic characterization of the heterojunctions, and data analysis. M.K. optimized the transfer technique. B.C. did the Raman and Pl characterizations. D.S. and S.M. developed the atomistic device model and performed the DFT–NEFG calculations. All author contributed in writing the manuscript.

ADDITIONAL INFORMATION

Supplementary Information accompanies the paper on the *npj 2D Materials and Applications* website (doi:10.1038/s41699-017-0017-3).

Competing interests: The authors declare no competing financial interests.

Publisher's note: Springer Nature remains neutral with regard to jurisdictional claims in published maps and institutional affiliations.

REFERENCES

1. Novoselov, K., Mishchenko, A., Carvalho, A. & Neto, A. C. 2D materials and van der Waals heterostructures. *Science* **353**, aac9439 (2016).
2. Das, S., Robinson, J. A., Dubey, M., Terrones, H. & Terrones, M. Beyond graphene: progress in novel two-dimensional materials and van der Waals solids. *Ann. Rev. Mater. Res.* **45**, 1–27 (2015).
3. Jariwala, D., Marks, T. J. & Hersam, M. C. Mixed-dimensional van der Waals heterostructures. *Nat. Mater.* **16**, 170–181 (2016).
4. Bablich, A., Kataria, S. & Lemme, M. C. Graphene and two-dimensional materials for optoelectronic applications. *Electronics* **5**, 13 (2016).
5. Roy, T. et al. Dual-gated MoS_2/WSe_2 van der Waals tunnel diodes and transistors. *ACS Nano* **9**, 2071–2079 (2015).
6. Zhang, K. et al. Interlayer transition and infrared photodetection in atomically thin type-ii $MoTe_2$/MoS_2 van der Waals heterostructures. *ACS Nano* **10**, 3852–3858 (2016).
7. Li, Y., Xu, C.-Y., Wang, J.-Y. & Zhen, L. Photodiode-like behavior and excellent photoresponse of vertical si/monolayer MoS_2 heterostructures. *Sci. Rep.* **4**, 7186 (2014).
8. Withers, F. et al. Light-emitting diodes by band-structure engineering in van der Waals heterostructures. *Nat. Mater.* **14**, 301–306 (2015).
9. Ross, J. S. et al. Electrically tunable excitonic light-emitting diodes based on monolayer WSe_2 pn junctions. *Nat. Nanotechnol.* **9**, 268–272 (2014).
10. Withers, F. et al. WSe_2 light-emitting tunneling transistors with enhanced brightness at room temperature. *Nano Lett.* **15**, 8223–8228 (2015).
11. Flöry, N. et al. A WSe_2/$MoSe_2$ heterostructure photovoltaic device. *Appl. Phys. Lett.* **107**, 123106 (2015).
12. Furchi, M. M., Pospischil, A., Libisch, F., Burgdoȉ'Lrfer, J. & Mueller, T. Photovoltaic effect in an electrically tunable van der Waals heterojunction. *Nano Lett.* **14**, 4785–4791 (2014).
13. Fogler, M., Butov, L. & Novoselov, K. High-temperature superfluidity with indirect excitons in van der Waals heterostructures. *Nat. Commun*. **5**, 4555 (2014).
14. Rivera, P. et al. Observation of long-lived interlayer excitons in monolayer $MoSe_2$–WSe_2 heterostructures. *Nat. Commun*. **6**, 6242 (2015).
15. Jariwala, D. et al. Hybrid, gate-tunable, van der Waals p–n heterojunctions from pentacene and MoS_2. *Nano Lett.* **16**, 497–503 (2015).
16. Jariwala, D. et al. Large-area, low-voltage, antiambipolar heterojunctions from solution-processed semiconductors. *Nano Lett.* **15**, 416–421 (2014).
17. Yi, S.-G. et al. Optoelectric properties of gate-tunable MoS_2/WSe_2 heterojunction. *IEEE Trans. Nanotechnol.* **15**, 499–505 (2016).
18. Wang, Z., He, X., Zhang, X.-X. & Alshareef, H. N. Hybrid van der Waals p–n heterojunctions based on SnO and 2D MoS_2. *Adv. Mater.* **28**, 9133–9141 (2016).
19. Li, Y. et al. Anti-ambipolar field-effect transistors based on few-layer 2D transition metal dichalcogenides. *ACS Appl. Mater. Interfaces* **8**, 15574–15581 (2016).
20. Jariwala, D. et al. Gate-tunable carbon nanotube–MoS_2 heterojunction pn diode. *Proc. Natl. Acad. Sci.* **110**, 18076–18080 (2013).
21. Kim, J.-K. et al. Trap-mediated electronic transport properties of gate-tunable pentacene/MoS_2 pn heterojunction diodes. *Sci. Rep*. **6**, 36775 (2016).
22. Cheng, R. et al. Electroluminescence and photocurrent generation from atomically sharp WSe_2/MoS_2 heterojunction p–n diodes. *Nano Lett.* **14**, 5590–5597 (2014).
23. Deng, Y. et al. Black phosphorus–monolayer MoS_2 van der Waals heterojunction p–n diode. *ACS Nano* **8**, 8292–8299 (2014).
24. Pezeshki, A., Shokouh, S. H. H., Nazari, T., Oh, K. & Im, S. Electric and photovoltaic behavior of a few-layer α-$MoTe_2$/MoS_2 dichalcogenide heterojunction. *Adv. Mater.* **28**, 3216–3222 (2016).
25. Lee, C.-H. et al. Atomically thin p–n junctions with van der Waals heterointerfaces. *Nat. Nanotechnol.* **9**, 676–681 (2014).
26. Kang, J., Tongay, S., Zhou, J., Li, J. & Wu, J. Band offsets and heterostructures of two-dimensional semiconductors. *Appl. Phys. Lett.* **102**, 012111 (2013).
27. Castellanos-Gomez, A. et al. Deterministic transfer of two-dimensional materials by all-dry viscoelastic stamping. *2D Materials* **1**, 011002 (2014).
28. Pradhan, N. R. et al. Field-effect transistors based on few-layered α-$MoTe_2$. *ACS Nano* **8**, 5911–5920 (2014).
29. Lin, Y.-F. et al. Ambipolar $MoTe_2$ transistors and their applications in logic circuits. *Adv. Mater.* **26**, 3263–3269 (2014).
30. Yin, Z. et al. Single-layer MoS_2 phototransistors. *ACS Nano* **6**, 74–80 (2011).
31. Late, D. J., Liu, B., Matte, H. R., Dravid, V. P. & Rao, C. Hysteresis in single-layer MoS_2 field effect transistors. *ACS Nano* **6**, 5635–5641 (2012).
32. Roy, K. et al. Graphene-MoS_2 hybrid structures for multifunctional photoresponsive memory devices. *Nat. Nanotechnol.* **8**, 826–830 (2013).
33. Li, X. et al. Persistent photoconductivity in two-dimensional Mo1- x $WxSe_2$–$MoSe_2$ van der Waals heterojunctions. *J. Mater. Res.* **31**, 923–930 (2016).
34. Wu, Y.-C. et al. Extrinsic origin of persistent photoconductivity in monolayer MoS_2 field effect transistors. *Sci. Rep*. **5**, 11472 (2015).
35. Li, T., Du, G., Zhang, B. & Zeng, Z. Scaling behavior of hysteresis in multilayer MoS_2 field effect transistors. *Appl. Phys. Lett.* **105**, 093107 (2014).
36. Atomistix ToolKit (ATK) with Virtual NanoLab, Version 2015.1, Last accessed_Dec. 2016, QuantumWise A/S, http://quantumwise.com/.
37. Perdew, J. P., Burke, K. & Ernzerhof, M. Generalized gradient approximation made simple. *Phys. Rev. Lett.* **77**, 3865 (1996).
38. Ozaki, T. Variationally optimized atomic orbitals for large-scale electronic structures. *Phys. Rev. B* **67**, 155108 (2003).
39. Ozaki, T. & Kino, H. Numerical atomic basis orbitals from h to kr. *Phys. Rev. B* **69**, 195113 (2004).
40. Grimme, S. Semiempirical GGA-type density functional constructed with a long-range dispersion correction. *J. Comput. Chem.* **27**, 1787–1799 (2006).
41. Brandbyge, M., Mozos, J.-L., Ordejón, P., Taylor, J. & Stokbro, K. Density-functional method for nonequilibrium electron transport. *Phys. Rev. B* **65**, 165401 (2002).
42. Stradi, D., Martinez, U., Blom, A., Brandbyge, M. & Stokbro, K. General atomistic approach for modeling metal-semiconductor interfaces using density functional theory and nonequilibrium Green's function. *Phys. Rev. B* **93**, 155302 (2016).
43. Soler, J. M. et al. The SIESTA method for ab initio order-n materials simulation. *J. Phys. Condens. Matter* **14**, 2745 (2002).
44. Zhang, Y. et al. Thickness considerations of two-dimensional layered semiconductors for transistor applications. *Sci. Rep*. **6**, 29615 (2016).
45. Yu, Y. et al. Equally efficient interlayer exciton relaxation and improved absorption in epitaxial and nonepitaxial MoS_2/WS_2 heterostructures. *Nano Lett.* **15**, 486–491 (2014).

Open Access This article is licensed under a Creative Commons Attribution 4.0 International License, which permits use, sharing, adaptation, distribution and reproduction in any medium or format, as long as you give appropriate credit to the original author(s) and the source, provide a link to the Creative Commons license, and indicate if changes were made. The images or other third party material in this article are included in the article's Creative Commons license, unless indicated otherwise in a credit line to the material. If material is not included in the article's Creative Commons license and your intended use is not permitted by statutory regulation or exceeds the permitted use, you will need to obtain permission directly from the copyright holder. To view a copy of this license, visit http://creativecommons.org/licenses/by/4.0/.

© The Author(s) 2017